Active Damping of LCL-Filter Resonance Using a Digital Resonant-Notch (Biquad) Filter

Pan, Donghua; Wang, Xiongfei; Blaabjerg, Frede; Gong, Hong

Published in:
Proceedings of 2018 20th European Conference on Power Electronics and Applications (EPE'18 ECCE Europe)

Publication date:
2018

Document Version
Accepted author manuscript, peer reviewed version

Active Damping of *LCL*-Filter Resonance Using a Digital Resonant-Notch (Biquad) Filter

Donghua Pan, Xiongfei Wang, Frede Blaabjerg, and Hong Gong
Department of Energy Technology, Aalborg University
Pontoppidanstraede 101, 9220
Aalborg, Denmark
Tel.: +45 – 5011 6068
Fax: +45 – 9815 1411
E-Mail: dop@et.aau.dk, xwa@et.aau.dk, fbl@et.aau.dk, hgo@et.aau.dk
URL: http://www.et.aau.dk/

Keywords

«Active damping», «Digital control», «Pulse Width Modulation (PWM)», «Robustness», «Voltage Source Inverters (VSI)».

Abstract

The *LCL* filter is a fundamental component which interfaces a voltage-source inverter (VSI) with a power grid, but on the other hand, it introduces a potential resonance risk which may be harmful to the system stability. In this paper, a digital biquad filter, which consists of a resonance and a notch, is proposed to damp the *LCL* resonance. By carefully tuning the resonance frequency and the notch frequency of the biquad filter, the *LCL* resonance is equivalently shifted from an unstable region into a stable one. The proposed method possesses a sensor-less benefit, and it can provide a high control bandwidth as well as a strong robustness. Experimental results acquired from a three-phase grid-connected inverter verify the effectiveness of the biquad filter.

1. Introduction

Nowadays, the increasing energy demand has stimulated a growing interest in distributed power generation system (DPGS) worldwide [1], [2]. As an efficient power conversion interface, the grid-connected pulse-width modulation (PWM) inverter with an *LCL* filter plays an important role in DPGS [3]. The *LCL* filter offers a cost-effective attenuation of the switching harmonics, but its resonance hazard may challenge the system stability, depending on the resonance frequency f_r as well as the computation and PWM delays [4], [5]. With a total delay of one and half sampling periods, a single grid current loop can stabilize the system without damping if $f_r > f_s/6$, where f_s is the sampling frequency [6]–[8]. While in the unstable region, i.e., $f_r < f_s/6$, damping solutions are required to avoid instability.

To avoid the attendant power loss with passive damping, active damping is usually favored. The typical active damping solutions are realized by compensating the control loop through feeding back the filter state variables, which might be the capacitor current [9]–[11], the capacitor voltage [12]–[15], and the grid current [16]–[18]. However, these solutions demand either an additional sensor (for the capacitor current) or a noise-sensitive derivative (for the capacitor voltage and the grid current), which are undesirable in practice. An alternative to these issues is to insert a digital filter, typically a notch filter, into the control loop to "filter" the resonance [19], [20]. By tuning the notch frequency at f_r, the *LCL* resonance can be fully cancelled. This yields a sensor-less benefit, but on the other hand, a poor sensitivity to the resonance drift [21], [22]. In [23], it is found that the notch frequency can be placed higher than f_r. The essence in this manner is to use the phase lag of the notch filter to push down the phase of the *LCL* filter, so as to avoid the −180º crossing at f_r. Unfortunately, the additional phase lag will impose a further limitation on the control bandwidth and thus degrade the control performance.

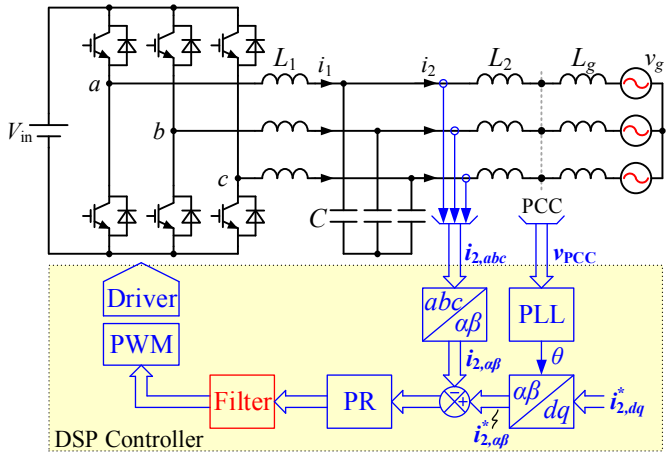

Fig. 1. Topology and current control architecture of a three-phase *LCL*-type grid-connected inverter.

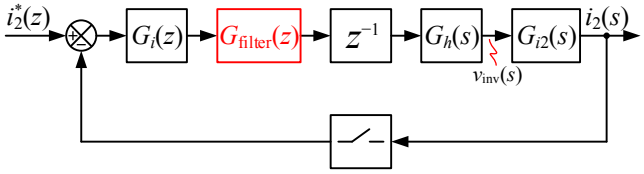

Fig. 2. Block diagram of the grid current control.

In this paper, a digital biquad filter, which consists of a resonance and a notch (anti-resonance), is adopted for damping the *LCL* resonance. By setting its notch frequency and resonance frequency below and above f_r, respectively, a constant 180º phase lead is introduced nearby f_r. This phase lead can equivalently shift the *LCL* resonance to a higher frequency above $f_s/6$, which thus falls into the stable region. As no phase lag is present, a high control bandwidth can be preserved. Moreover, with a careful tuning of the biquad filter, a high robustness is acquired to tolerate the wide-range resonance drift, which may be caused by the filter parameter deviation as well as the grid impedance variation.

This paper begins with a description and modeling of the *LCL*-type grid-connected inverter in Section 2. This is followed by the proposed biquad filter active damping in Section 3. Basic principle and digital implementation of the biquad filter are elaborated in this section. A co-design of the current regulator and the active damping is discussed in Section 4. Two sets of controller parameters are tuned according to the stiffness of the power grid. Experimental results are provided to confirm the theoretical expectations in Section 5. Finally, Section 6 concludes this paper.

2. System Description and Modeling

Fig. 1 shows a three-phase voltage-source inverter (VSI) feeding into the grid through an *LCL* filter. L_1 is the inverter-side inductor, C is the filter capacitor, and L_2 is the grid-side inductor. L_g is the grid inductance at the point of common coupling (PCC). The PCC voltage v_{PCC} is sensed and fed to a phase-locked loop (PLL) for grid synchronization. The grid current i_2 is controlled with a proportional-resonant (PR) regulator in the stationary $\alpha\beta$ frame. A digital filter is cascaded to the PR regulator for the damping purpose, and its output is fed to a digital PWM modulator to generate inverter driver signals.

The digital modulator contains computation and PWM delays [24], [25]. A block diagram that accounts for these delays is shown in Fig. 2, where $G_i(z)$ is the PR regulator, $G_{filter}(z)$ is the digital filter, z^{-1} represents the one-sample computational delay, and $G_h(s)$ is the transfer function of the zero-order hold (ZOH) which causes the half-sample PWM delay, expressed as

$$G_h(s) = \frac{1 - e^{-sT_s}}{s} \tag{1}$$

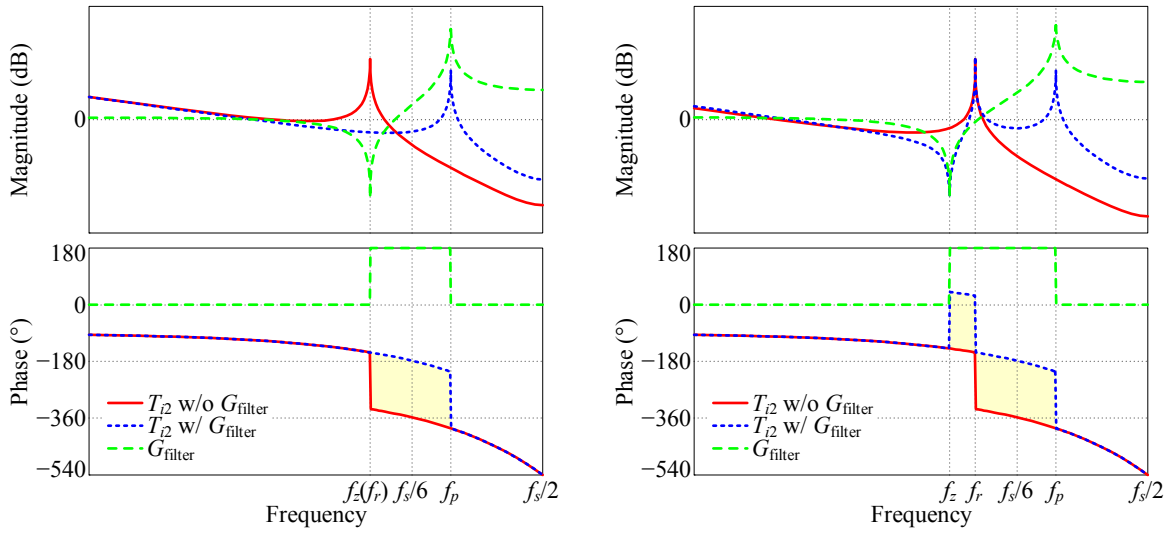

Fig. 3. Bode diagrams of the loop gain and the biquad filter. (a) $f_z = f_r$. (b) $f_z < f_r$.

where T_s is the sampling period. $G_{i2}(s)$ is the transfer function from the inverter output voltage $v_{inv}(s)$ to $i_2(s)$, and it is expressed as

$$G_{i2}(s) = \frac{i_2(s)}{v_{inv}(s)} = \frac{1}{s(L_1 + L_2 + L_g)} \cdot \frac{\omega_r^2}{s^2 + \omega_r^2} \tag{2}$$

where ω_r is the *LCL* resonance angular frequency and expressed as

$$\omega_r = 2\pi f_r = \sqrt{\frac{L_1 + L_2 + L_g}{L_1(L_2 + L_g)C}}. \tag{3}$$

To perform an accurate stability analysis in the z-domain, the system discrete loop gain $T_{i2}(z)$ is derived by applying the ZOH transform to $G_{i2}(s)$, i.e.,

$$\begin{aligned} T_{i2}(z) &= z^{-1} G_i(z) G_{filter}(z) Z_{ZOH}\left[G_{i2}(s)\right] \\ &= \frac{G_i(z) G_{filter}(z)}{\omega_r(L_1 + L_2 + L_g)} \cdot \frac{\omega_r T_s\left(z^2 - 2z\cos\omega_r T_s + 1\right) - (z-1)^2 \sin\omega_r T_s}{z(z-1)\left(z^2 - 2z\cos\omega_r T_s + 1\right)} \cdot \end{aligned} \tag{4}$$

3. Resonant-Notch (Biquad) Filter Active Damping

3.1. Basic Ideal of the Proposed Method

Before drawing the digital filter, the system without it, i.e., $G_{filter}(z) = 1$, is revisited at first. Fig. 3(a) shows the Bode diagram of $T_{i2}(z)$ with $G_{filter}(z) = 1$, where two resonance frequencies around $f_s/6$ are depicted for comparison. For $f_r < f_s/6$ (see the solid line), the phase plot crosses over −180° at f_r with an infinite resonance peak, implying the instability. For $f_r > f_s/6$ (see the dashed line), the phase lag created by the time delay causes the phase plot to cross over −180° at $f_s/6$ in advance. Thus, the single grid current loop can be stabilized as long as the *gain margin* at $f_s/6$ is greater than 0 dB. While the resonance peak at f_r needs not to be damped, since the phase is already well below −180° at this frequency.

As the stability is highly related to f_r, a natural question coming to mind is whether it is possible to shift f_r from the unstable region into the stable one. Achieving this goal, in the gain aspect, requires to cancel

out the original resonance and then create a new one at the destination frequency. Meanwhile, in the phase aspect, a constant 180º phase lead is demanded between the original and destination resonance frequencies, shown as the shaded area in Fig. 3(a). Obviously, these requirements can be satisfied with a biquad filter, which is expressed as

$$G_{\text{filter}}(s)=\frac{\omega_p^2}{\omega_z^2}\cdot\frac{s^2+\omega_z^2}{s^2+\omega_p^2} \tag{5}$$

where $\omega_p = 2\pi f_p$ and $\omega_z = 2\pi f_z$ are the frequencies of the resonant poles and zeros, respectively, and a constant coefficient ω_p^2/ω_z^2 is incorporated to ensure an unity dc gain. The frequency response of the biquad filter is also depicted in Fig. 3(a). As seen, its magnitude yields a notch at f_z and a resonance at f_p, and its phase keeps 180º in the range (f_z, f_p) and changes to zero outside this range. Therefore, to perform an ideal resonance shift, f_z is set at f_r to cancel out the original resonance, and f_p is the destination resonance frequency, which should be located in the stable region, i.e., (f_s/6, f_s/2). This resonance shift can also be identified in the transfer function by multiplying $G_{i2}(s)$ with $G_{\text{filter}}(s)$ under $f_z = f_r$, i.e.,

$$G_{i2}(s)\cdot G_{\text{filter}}(s)\Big|_{\omega_z=\omega_r}=\frac{1}{s\left(L_1+L_2+L_g\right)}\frac{\omega_r^2}{s^2+\omega_r^2}\cdot\frac{\omega_p^2}{\omega_z^2}\frac{s^2+\omega_z^2}{s^2+\omega_p^2}\Bigg|_{\omega_z=\omega_r}=\frac{1}{s\left(L_1+L_2+L_g\right)}\frac{\omega_p^2}{s^2+\omega_p^2} \tag{6}$$

However, in practice, f_r may vary in a wide range due to the variations of filter parameters and grid impedance, which makes it difficult to realize $f_z = f_r$ in the controller. This fortunately can be resolved by noting that a lower f_z is also proper. Since the phase plot of $T_{i2}(z)$ no longer crosses over −180º at f_r after compensating with the biquad filter, there is actually no need to cancel out the original resonance, and f_z can be placed below f_r. The Bode diagram with $f_z < f_r$ is depicted in Fig. 3(b). Observing Figs. 3(a) and (b), it can be found that the −180º crossings in both cases are raised from f_r to f_s/6, owing to the 180º phase lead offered by the biquad filter. Therefore, the stability requirement in both cases will be a positive gain margin at f_s/6, which is exactly the same as that for $f_r > f_s$/6. That means, the resonance "shift" is also obtained with $f_z < f_r$, from the control perspective.

From the above analysis, the constraints of the biquad filter are summarized as

$$f_z \le f_r \text{, and } f_s/6 < f_p < f_s/2\,. \tag{7}$$

To be robust, f_z can be tuned at the possible lowest value that f_r may reach. Recalling (3), f_r decreases with the increase of L_g. Thus, f_z can be placed at f_r under the infinite L_g, which is exactly the resonance frequency between L_1 and C, i.e.,

$$f_z = f_r\big|_{L_g\to\infty}=\frac{1}{2\pi\sqrt{L_1C}}\triangleq f_{L1C}\,. \tag{8}$$

3.2. Discretization of the Biquad Filter

For digital implementation, the biquad filter $G_{\text{filter}}(s)$ needs to be discretized. As its resonance frequency f_p and notch frequency f_z are the most important terms of concern, they should remain unchanged after discretization. For this purpose, the pole-zero matching discretization is applied, which leads to

$$G_{\text{filter}}(z)=\frac{\omega_p^2}{\omega_z^2}\cdot\frac{z^2-2z\cos\omega_z T_s+1}{z^2-2z\cos\omega_p T_s+1}\,. \tag{9}$$

Frequency responses of $G_{\text{filter}}(s)$ and $G_{\text{filter}}(z)$ with f_s = 10 kHz are depicted in Fig. 4. It can be observed that the digital biquad filter exhibits well-matched characteristics as the continuous one.

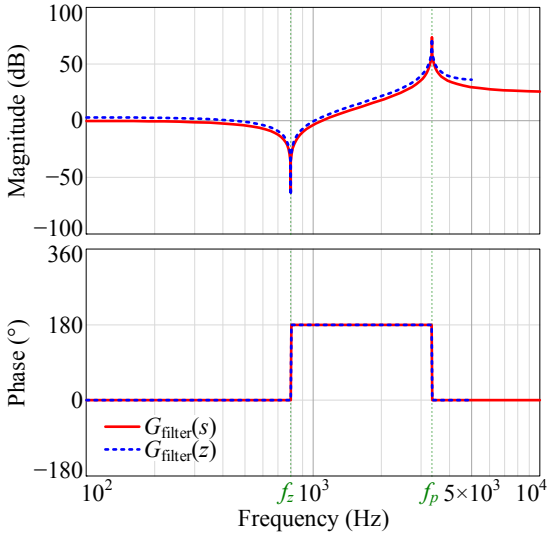

Fig. 4. Bode diagrams of $G_{filter}(s)$ and $G_{filter}(z)$.

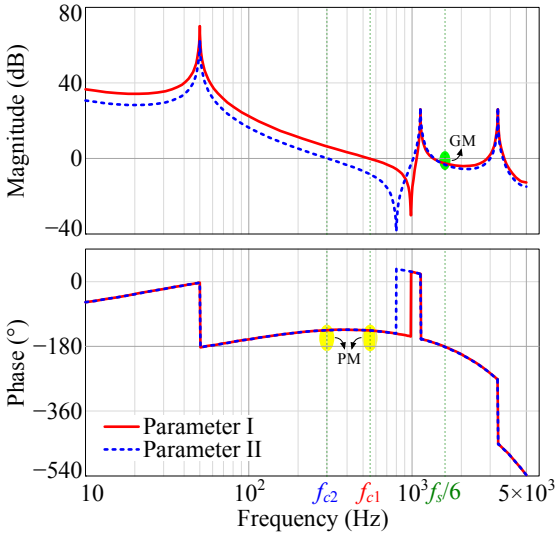

Fig. 5. Bode diagrams of compensated loop gain.

TABLE I. Parameters of the Prototype

Parameter	Symbol	Value	Parameter	Symbol	Value
Input voltage	V_{in}	650 V	Inverter-side inductor	L_1	2 mH
Grid voltage	V_g	400 V	Grid-side inductor	L_2	2 mH
Output power	P_o	5 kW	Filter capacitor	C	20 μF
Fundamental frequency	f_0	50 Hz	Resonance frequency	f_r	1.13 kHz
Switching frequency	f_{sw}	10 kHz	Sampling frequency	f_s	10 kHz

4. Co-design of Current Regulator and Active Damping

In the proposed control scheme, the PR regulator $G_i(z)$ and the biquad filter $G_{filter}(z)$ are cascaded to form the high-order digital controller, and they should be designed together to ensure a satisfactory dynamic with reasonable stability margins. The design procedure is based on the prototype parameters listed in Table I, where the *LCL* filter is designed with the well-known constraints in [26], and its consequent resonance frequency f_r = 1.13 kHz is lower than $f_s/6$ (1.67 kHz).

For the PR regulator, its expressions before and after applying prewarped Tustin transform are given as

$$G_i(s) = K_p + \frac{K_r s}{s^2 + \omega_0^2} \tag{10}$$

$$G_i(z) = K_p + K_r \frac{\sin \omega_0 T_s}{2\omega_0} \frac{z^2 - 1}{z^2 - 2z\cos \omega_0 T_s + 1} \tag{11}$$

where $\omega_0 = 2\pi f_0$ is the fundamental angular frequency. The proportional gain K_p and the resonant gain K_r are tuned according to the desired crossover frequency f_c and the phase margin (PM). Besides, K_p is also constrained by the gain margin (GM). As discussed above, a positive (typically 3 dB) GM at $f_s/6$ ($GM_{fs/6}$) is required, and from (4) and (9), its expression is derived as

$$\begin{aligned} GM_{fs/6} &= -20\lg\left|T_{i2}\left(e^{j\pi/3}\right)\right| \\ &= 20\lg\left|\frac{1}{K_p}\cdot\frac{\omega_z^2\left(1-2\cos\omega_p T_s\right)}{\omega_p^2\left(1-2\cos\omega_z T_s\right)}\cdot\frac{\omega_r\left(L_1+L_2+L_g\right)\left(1-2\cos\omega_r T_s\right)}{\sin\omega_r T_s+\omega_r T_s\left(1-2\cos\omega_r T_s\right)}\right|. \end{aligned} \tag{12}$$

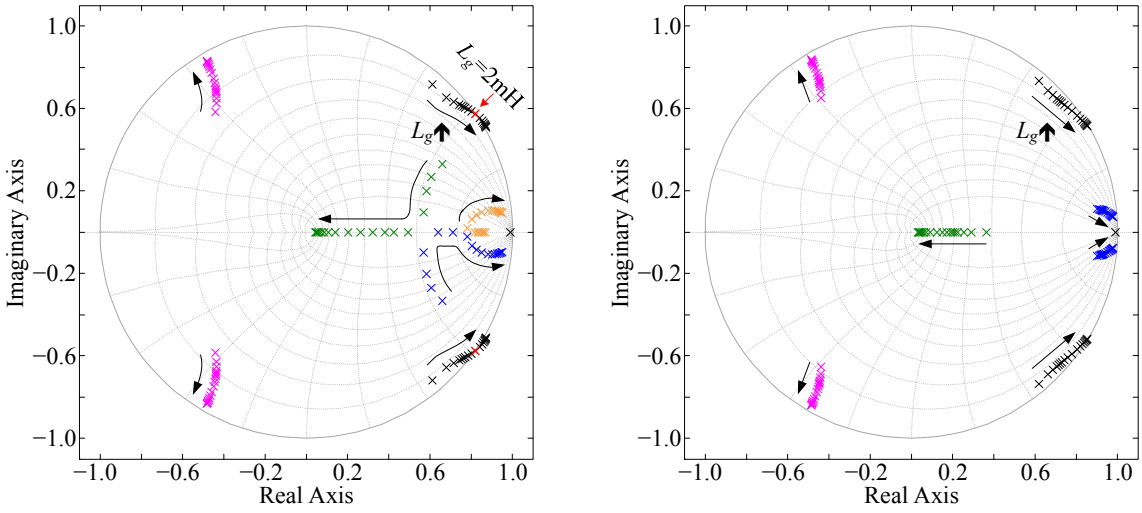

Fig. 6. Closed-loop pole maps with L_g varying up to 10 mH. (a) Parameter I: K_p = 10, K_r = 1×10^4, f_p = 3.3 kHz, and f_z = 980 Hz. (b) Parameter II: K_p = 5, K_r = 5×10^3, f_p = 3.3 kHz, and f_z = 800 Hz.

From (12), it can be found that the design of K_p is related to f_p and f_z. Recalling (7), f_p is limited to the range (f_s/6, f_s/2) for a stable operation. Here, the middle value $f_p = f_s/3$ = 3.3 kHz is chosen. f_z should be selected considering the possible variation of f_r, which mainly depends on the grid impedance, or in other words, the stiffness of the power grid.

4.1. Design in Stiff Grid (Parameter I)

In the stiff grid condition, the effect of L_g is negligible, and the variation of f_r is mainly caused by the filter parameter deviations. Typically, the variations of inductance and capacitance are limited to ±20% and ±10%, respectively. Thus, referring to (3), the lowest f_r is calculated as

$$f_{r,\min} = \frac{1}{2\pi}\sqrt{\frac{1.2L_1 + 1.2L_2}{1.2L_1 \cdot 1.2L_2 \cdot 1.1C}} = 0.87 \cdot \frac{1}{2\pi}\sqrt{\frac{L_1 + L_2}{L_1 L_2 C}}\,. \tag{13}$$

which is 0.87 of its nominal value. Hence, $f_z = 0.87 f_r$ = 980 Hz is set. Substituting f_p, f_z, and the system parameters into (12) and letting $\mathrm{GM}_{\mathrm{fs/6}} \geq 3$ dB, $K_p \leq 10.1$ is yielded. Here, K_p = 10 is chosen to maximize the control bandwidth. Afterwards, K_r = 1×10^4 is designed for a target PM of 45º.

4.2. Design in Weak Grid (Parameter II)

In weak grid condition, L_g, and thus f_r, can vary in a wide range. As suggested in (8), $f_z = f_{L1C}$ = 800 Hz is set in this case. Substituting f_p, f_z, and the system parameters into (12) and then letting $\mathrm{GM}_{\mathrm{fs/6}} \geq 3$ dB, $K_p \leq 5.5$ is yielded. Likewise, K_p = 5 and K_r = 5×10^3 are designed successively, which are exactly halves of those designed in stiff grid due to the decrease of f_z.

For convenience of illustrattion, the above two sets of controller parameters are referred to as Parameter I and Parameter II, based on which the Bode diagrams of the compensated loop gain are given in Fig. 5. For Parameter I, the crossover frequency f_{c1} = 550 Hz, PM = 45º, and GM = 3.1 dB; for Parameter II, the crossover frequency f_{c2} = 300 Hz, PM = 45º, and GM = 3.5 dB. All the stability constraints are well satisfied in both cases, and a higher control bandwidth is preserved with Parameter I.

The control bandwidth with Parameter II is degraded, but its robustness is not trivial. Recalling (4), Fig. 6 depicts the closed-loop pole maps with L_g varying up to 10% per unit, which corresponds to 10 mH in the test system. As shown in Fig. 6(a), the resonant poles with Parameter I move outside the unit circle for $L_g \geq 2$ mH. This is because that f_r falls below 975 Hz with $L_g \geq 2$ mH, lower than f_z (980 Hz), and the requirement of $f_z \leq f_r$ is no longer satisfied. However, with Parameter II, as shown in Fig. 6(b), all the closed-loop poles stay inside the unit circle irrespective of L_g, which implies a high robustness.

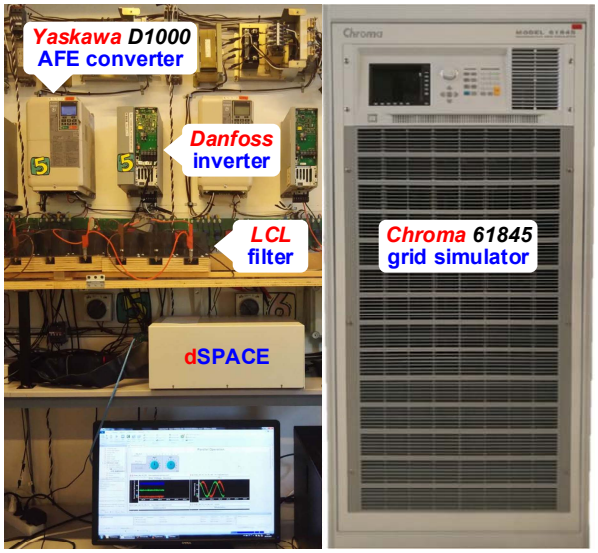

Fig. 7. Experimental platform with a grid-connected inverter and a grid simulator.

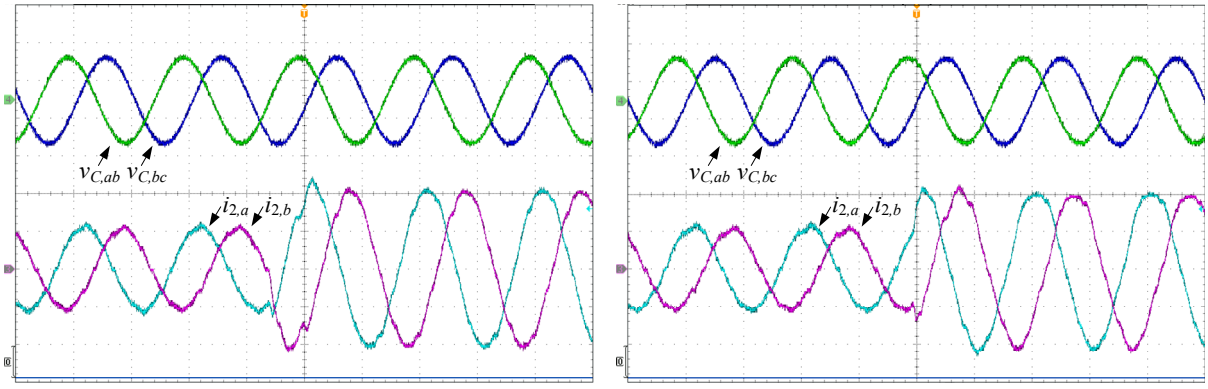

(a) (b)

Fig. 8. Experimental results when current reference steps from half to full load at $L_g = 0$. (a) Parameter I: $K_p = 10$, $K_r = 1\times10^4$, $f_p = 3.3$ kHz, and $f_z = 980$ Hz. (b) Parameter II: $K_p = 5$, $K_r = 5\times10^3$, $f_p = 3.3$ kHz, and $f_z = 800$ Hz. Voltage scale: 500 V/div, current scale: 5 A/div, time scale: 10 ms/div.

5. Experimental Verification

A three-phase prototype of Fig. 1 is built in the lab based on the parameters listed in Table I. Its photograph is given in Fig. 7. The control scheme is implemented with a dSPACE DS1007 platform, whose output PWM signals are channeled through fiber optic cables to a Danfoss VLT FC-103P11K inverter. The inverter is supplied by a Yaskawa D1000 active-front-end (AFE) converter, and its output is connected to a Chroma 61845 grid simulator simulating different grid conditions.

Based on this platform, experimental results acquired with the two sets of controller parameters are compared here. The capacitor voltage v_C and the grid current i_2 are both measured. Fig. 8 shows the experimental results when the current reference steps from half to full load at $L_g = 0$. Stable operations are retained for both sets of controller parameters, while a smoother steady-state waveform and a faster transient response are obtained with Parameter I, due to its relatively higher control bandwidth.

Fig. 9 shows the experimental results where $L_g = 2$ mH. For Parameter I, oscillations are triggered when L_g is changing from 0 to 2 mH, implying instability. For Parameter II, the stable operation is maintained irrespective of L_g, implying a robust design. The experimental result are consistent with the theoretical analysis in Section 4, and they verify the effectiveness of the proposed biquad filter active damping.

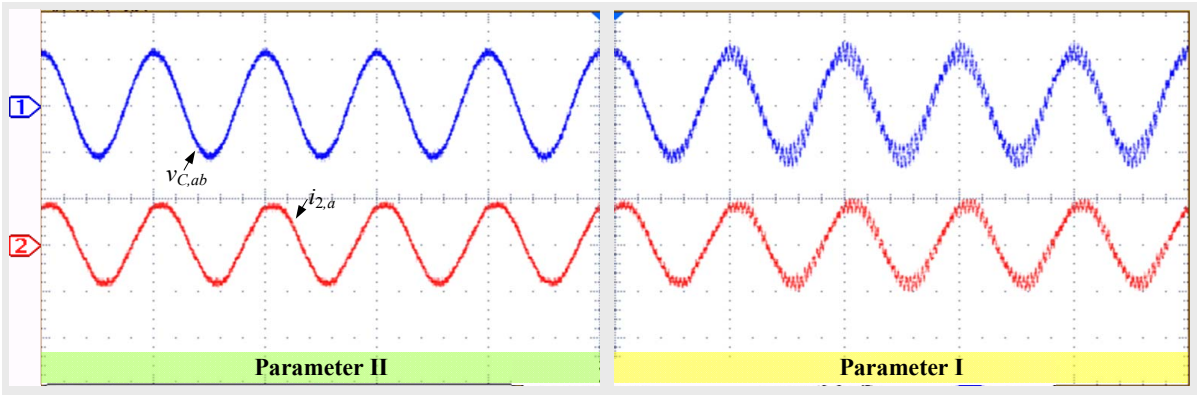

Fig. 9. Experimental results under L_g = 2 mH. Voltage scale: 500 V/div, current scale: 5 A/div, time scale: 10 ms/div.

6. Conclusion

A resonant-notch (biquad) filter active damping is proposed in this paper for the *LCL*-type grid-connected inverter. With the help of the 180º phase lead introduced by the biquad filter, the *LCL* resonance can be equivalently shifted from the unstable region into the stable one. Basic principle and digital implementation of the biquad filter are discussed. Design procedures are presented to achieve a high control bandwidth and a strong robustness. The effectiveness of the proposed method is verified by experimental results from a three-phase grid-connected inverter.

References

[1] F. Blaabjerg, Y. Yang, D. Yang, and X. Wang, "Distributed power-generation systems and protection," *Proc. IEEE*, vol. 105, no. 7, pp. 1311−1331, Jul. 2017.

[2] X. Wang and F. Blaabjerg, "Harmonic stability in power electronic based power systems: concept, modeling, and analysis," *IEEE Trans. Smart Grid*, to be published.

[3] X. Ruan, X. Wang, D. Pan, D. Yang, W. Li, and C. Bao, *Control Techniques for LCL-Type Grid-Connected Inverters*. Singapore: Springer, 2017.

[4] L. Harnefors, A. G. Yepes, A. Vidal, and J. D. Gandoy, "Passivity-based controller design of grid-connected VSCs for prevention of electrical resonance instability," *IEEE Trans. Ind. Electron.*, vol. 62, no. 2, pp. 702−710, Feb. 2015.

[5] L. Harnefors, X. Wang, A. G. Yepes, and F. Blaabjerg, "Passivity-based stability assessment of grid-connected VSCs − an overview," *IEEE J. Emerg. Sel. Topics Power Electron.*, vol. 4, no. 1, pp. 116−125, Mar. 2016.

[6] S. G. Parker, B. P. McGrath, and D. G. Holmes, "Regions of active damping control for *LCL* filters," *IEEE Trans. Ind. Appl.*, vol. 50, no. 1, pp. 424−432, Jan./Feb. 2014.

[7] J. Wang, J. D. Yan, L. Jiang, and J. Zou, "Delay-dependent stability of single-loop controlled grid-connected inverters with *LCL* filters," *IEEE Trans. Power Electron.*, vol. 31, no. 1, pp. 743−757, Jan. 2016.

[8] X. Wang, F. Blaabjerg, and P. C. Loh, "Passivity-based stability analysis and damping injection for multi-paralleled voltage source converters with *LCL* filters," *IEEE Trans. Power Electron.*, vol. 32, no. 11, pp. 8922−8935, Nov. 2017.

[9] D. Pan, X. Ruan, C. Bao, W. Li, and X. Wang, "Capacitor-current-feedback active damping with reduced computation delay for improving robustness of *LCL*-type grid-connected inverter," *IEEE Trans. Power Electron.*, vol. 29, no. 7, pp. 3414−3427, Jul. 2014.

[10] D. Pan, X. Ruan, C. Bao, W. Li, and X. Wang, "Optimized controller design for *LCL*-type grid-connected inverter to achieve high robustness against grid-impedance variation," *IEEE Trans. Ind. Electron.*, vol. 62, no. 3, pp. 1537−1547, Mar. 2015.

[11] D. Pan, X. Ruan, X. Wang, H. Yu, and Z. Xing, "Analysis and design of current control schemes for *LCL*-type grid-connected inverter based on a general mathematical model," *IEEE Trans. Power Electron.*, vol. 32, no. 6, pp. 4395−4410, Jun. 2017.

[12] J. Dannehl, F. W. Fuchs, S. Hansen, and P. B. Thøgersen, "Investigation of active damping approaches for PI-based current control of grid-connected pulse width modulation converters with *LCL* filters," *IEEE Trans. Ind. Appl.*, vol. 46, no. 4, pp. 1509−1517, Jul./Aug. 2010.

[13] R. P. Alzola, M. Liserre, F. Blaabjerg, R. Sebastián, J. Dannehl, and F. W. Fuchs, "Systematic design of the lead-lag network method for active damping in *LCL*-filter based three phase converters," *IEEE Trans. Ind. Informat.*, vol. 10, no. 1, pp. 43−52, Feb. 2014.

[14] Z. Xin, P. C. Loh, X. Wang, F. Blaabjerg, and Y. Tang, "Highly accurate derivatives for *LCL*-filtered grid converter with capacitor voltage active damping," *IEEE Trans. Power Electron.*, vol. 31, no. 5, pp. 3612−3625, May. 2016.

[15] D. Pan, X. Ruan, and X. Wang, "Direct realization of digital differentiators in discrete domain for active damping of *LCL*-type grid-connected inverter," *IEEE Trans. Power Electron.*, to be published.

[16] M. Hanif, V. Khadkikar, W. Xiao, and J. L. Kirtley, "Two degrees of freedom active damping technique for *LCL* filter-based grid connected PV systems," *IEEE Trans. Ind. Electron.*, vol. 61, no. 6, pp. 2795−2803, Jun. 2014.

[17] J. Xu, S. Xie, and T. Tang, "Active damping-based control for grid-connected *LCL*-filtered inverter with injected grid current feedback only," *IEEE Trans. Ind. Electron.*, vol. 61, no. 9, pp. 4746−4758, Sep. 2014.

[18] X. Wang, F. Blaabjerg, and P. C. Loh, "Grid-current-feedback active damping for *LCL* resonance in grid-connected voltage source converters," *IEEE Trans. Power Electron.*, vol. 31, no. 1, pp. 213−223, Jan. 2016.

[19] J. Dannehl, M. Liserre, and F. W. Fuchs, "Filter-based active damping of voltage source converters with *LCL* filter," *IEEE Trans. Ind. Electron.*, vol. 58, no. 8, pp. 3623−3633, Aug. 2011.

[20] S. Zhang, S. Jiang, X. Lu, B. Ge, and F. Z. Peng, "Resonance issues and damping techniques for grid-connected inverters with long transmission cable," *IEEE Trans. Power Electron.*, vol. 29, no. 1, pp. 110−120, Jan. 2014.

[21] M. Liserre, R. Teodorescu, and F. Blaabjerg, "Stability of photovoltaic and wind turbine grid-connected inverters for a large set of grid impedance values," *IEEE Trans. Power Electron.*, vol. 21, no. 1, pp. 263−272, Jan. 2006.

[22] R. P. Alzola, M. Liserre, F. Blaabjerg, M. Ordonez, and T. Kerekes, "A self-commissioning notch filter for active damping in a three-phase *LCL*-filter- based grid-tie converter," *IEEE Trans. Power Electron.*, vol. 29, no. 12, pp. 6754−6761, Dec. 2014.

[23] W. Yao, Y. Yang, X. Zhang, F. Blaabjerg, and P. C. Loh, "Design and analysis of robust active damping for *LCL* filters using digital notch filters," *IEEE Trans. Power Electron.*, vol. 32, no. 3, pp. 2360−2375, Mar. 2017.

[24] D. G. Holmes, T. A. Lipo, B. P. McGrath, and W. Y. Kong, "Optimized design of stationary frame three phase AC current regulators," *IEEE Trans. Power Electron.*, vol. 24, no. 11, pp. 2417−2426, Nov. 2009.

[25] D. Pan, X. Ruan, X. Wang, F. Blaabjerg, X. Wang, and Q. Zhou, "A highly robust single-loop current control scheme for grid-connected inverter with an improved *LCCL* filter configuration," *IEEE Trans. Power Electron.*, to be published.

[26] D. Pan, X. Ruan, C. Bao, W. Li, and X. Wang, "Magnetic integration of the *LCL* filter in grid-connected inverters," *IEEE Trans. Power Electron.*, vol. 29, no. 4, pp. 1573−1578, Apr. 2014.